COMPUTATIONAL PHANTOM FOR A 5-YEAR OLD CHILD RED BONE MARROW DOSIMETRY DUE TO INCORPORATED BETA EMITTERS

Sharagin PA[1] ✉, Tolstykh EI[1], Shishkina EA[1,2]

[1] Urals Research Center for Radiation Medicine of the Federal Medical-Biological Agency, Chelyabinsk, Russia
[2] Chelyabinsk State University, Chelyabinsk, Russia

The red bone marrow (RBM) exposure due to bone-seeking radionuclides can lead to grave medical consequences. In particular, the increased risk of leukemia in people exposed due to contamination of the Techa River in 1950s is associated with the RBM exposure due to ^{89,90}Sr. Improvement of the internal RBM dosimetry methods includes the development of computational phantoms that represent 3D models of the skeletal sites. Modeling radiation transport within such phantoms enables estimation of conversion factors from the radionuclide activity in the bone to the RBM dose rate. This paper is an extension study focused on generating a set of computational phantoms representing skeletons of individuals of different ages. The aim was to develop a computational phantom representing a 5-year-old child for internal RBM dosimetry from incorporated beta emitters. The phantoms of the skeletal sites with active hematopoiesis were created using the original Stochastic Parametric Skeletal Dosimetry (SPSD) method. With this method, every such site represented a set of smaller phantoms of simple geometric shape. RBM distribution across the skeleton, bone size, characteristics of bone micro-architecture, as well as density and chemical composition of the simulated media (RBM, bone) were determined based on the published data. As a result, a computational phantom of the major skeletal sites with active hematopoiesis representing a 5-year-old child was generated that included 43 phantoms of bone fragments. Linear dimensions of phantoms were within 3–75 mm. Micro-architecture parameters varied greatly: *BV/TV* ratio —13–52%, *Tb. Th*. — 0.09–0.29 mm, *Tb. Sp*. —0.48–0.98 mm.

Keywords: trabecular bone, cortical bone, bone marrow dosimetry, computational phantoms, Sr

Funding: the study was performed within the framework of the Federal Targeted Program "Ensuring Nuclear and Radiation Safety for 2016–2020 and for the Period up to 2035" and supported by the Federal Medical Biological Agency of Russia.

Author contribution: Sharagin PA — data acquisition, analysis and interpretation, manuscript writing and editing; Tolstykh EI — developing the research method; Shishkina EA — developing the concept, manuscript editing.

✉ **Correspondence should be addressed:** Pavel A. Sharagin
Vorovskogo, 68-a, Chelyabinsk, 454141, Russia; sharagin@urcrm.ru

Received: 23.10.2023 **Accepted:** 05.12.2023 **Published online:** 31.12.2023

DOI: 10.47183/mes.2023.061

ВЫЧИСЛИТЕЛЬНЫЙ ФАНТОМ ДЛЯ ДОЗИМЕТРИИ КРАСНОГО КОСТНОГО МОЗГА ПЯТИЛЕТНЕГО РЕБЕНКА ОТ ИНКОРПОРИРОВАННЫХ БЕТА-ИЗЛУЧАТЕЛЕЙ

П. А. Шарагин[1] ✉, Е. И. Толстых[1], Е. А. Шишкина[1,2]

[1] Уральский научно-практический центр радиационной медицины Федерального медико-биологического агентства России, Челябинск, Россия

[2] Челябинский государственный университет, Челябинск, Россия

Облучение ККМ (красного костного мозга) остеотропными радионуклидами может приводить к серьезным медицинским последствиям. В частности, увеличение риска развития лейкозов у людей, подвергшихся радиационному воздействию в результате загрязнения реки Течи в 1950-е гг., связано с облучением ККМ от ^{89,90}Sr. Совершенствование методов внутренней дозиметрии ККМ включает разработку вычислительных фантомов, которые представляют собой трехмерные модели участков скелета. Моделирование переноса излучений внутри таких фантомов позволяет оценить коэффициенты перехода от активности радионуклида в кости к мощности дозы в ККМ. Настоящая статья — продолжение работы по созданию набора вычислительных фантомов скелета для людей разного возраста. Цель: разработать вычислительный фантом скелета пятилетнего ребенка для внутренней дозиметрии ККМ от инкорпорированных бета-излучателей. Фантомы участков скелета с активным гемопоэзом создавали с использованием оригинальной методики SPSD (stochastic parametric skeletal dosimetry). В рамках этой методики каждый такой участок представлял собой набор меньших фантомов простой геометрической формы. Распределение ККМ в скелете, размеры костей, характеристики костной микроархитектуры, а также плотность и химический состав моделируемых сред (ККМ, кость) определяли на основе опубликованных данных. В результате был сгенерирован вычислительный фантом основных участков скелета с активным гемопоэзом для пятилетнего ребенка, включающий 43 фантома участков костей. Линейные размеры фантомов были в пределах от 3 мм до 75 мм. Параметры микроархитектуры варьировали в широких пределах: отношение *BV/TV* — от 13% до 52%, *Tb. Th.* — от 0,09 мм до 0,29 мм, *Tb. Sp*. — от 0,48 мм до 0,98 мм.

Ключевые слова: трабекулярная кость, кортикальная кость, дозиметрия костного мозга, вычислительные фантомы, Sr

Финансирование: работа выполнена в рамках реализации Федеральной целевой программы «Обеспечение ядерной и радиационной безопасности на 2016–2020 годы и на период до 2035 года» и при финансовой поддержке Федерального медико-биологического агентства России.

Вклад авторов: П. А. Шарагин — получение, анализ и интерпретация данных, написание и редактирование статьи; Е. И. Толстых — разработка методики исследования, редактирование статьи; Е. А. Шишкина — разработка концепции, редактирование статьи.

✉ **Для корреспонденции:** Павел Алексеевич Шарагин
ул. Воровского, д. 68-а, г. Челябинск, 454141, Россия; sharagin@urcrm.ru

Статья получена: 23.10.2023 **Статья принята к печати:** 05.12.2023 **Опубликована онлайн:** 31.12.2023

DOI: 10.47183/mes.2023.061

After entering the body, bone-seeking radionuclides accumulate in the mineralized bone tissue and cause local red bone marrow (RBM) exposure, which can lead to grave medical consequences. Thus, for example, the increased risk of leukemia and the development of chronic radiation syndrome in people from the cohort of the Techa River contaminated with radionuclides in 1950s are largely attributed to ingestion of strontium isotopes (^{89,90}Sr) [1–4]. It was strontium isotopes that were the main sources of the RBM internal exposure in these people. Thus, improvement of dosimetry methods for

bone-seeking radionuclides can help prepare for potential emergency situations related to radioactive contamination of the environment and represents an important challenge of radiobiology and radiation protection. Biokinetic and dosimetric models are used to estimate the absorbed dose to RBM. Biokinetic ones are used to assess specific radionuclide activity in the source tissue (skeletal bones). Such models simulate metabolic processes in the body allowing one to estimate the ingested radionuclide fraction in various organs, particularly in the bones, depending on its quantity and time after ingestion [5]. The dose conversion factors (DF) for conversion of specific radionuclide activity in the source tissue (skeleton) into the absorbed dose rate in the target tissue (RBM) are used to calculate the dose to RBM. DF represents a dosimetric model output. The computational skeletal dosimetry phantoms representing surrogates of real body tissues and describing relative positions of the source (bone) and target (RBM) tissues, in which radiation transport is simulated, are used to simulate the exposure geometry. The existing computational phantoms for RBM dosimetry are based on the analysis of a limited number of post mortem bone CT images [6–12]. The use of such phantoms makes it impossible to consider individual variability in bone size and microstructure, as well as the associated uncertainty in the DF estimates. As an alternative, Stochastic Parametric Skeletal Dosimetry (SPSD) modeling, the original parametric method for stochastic bone structure modeling, was developed in the Urals Research Center for Radiation Medicine [13, 14]. The SPSD phantom parameters are based on the numerous published measurement results of real bones in people of different ages. A lot of statistics reported in the papers used enable estimation of uncertainties associated with individual variability in the skeletal parameters. A phantom is a virtual model of simple geometric shape. A computational phantom is filled with spongiosa (a combination of trabecular bone and bone marrow) and covered with a dense layer of cortical bone. RBM, trabecular bone and cortical bone were modeled as distinct media constituting the phantom. Such complex model is a simplified representation of the real bone that is well suited for internal dosimetry from the bone-seeking beta emitters [13, 14]. The model consistency was demonstrated in the reported numerical experiments [13, 15, 16] yielding the energy curves for SPSD phantoms that were matched to the published data.

When the environment is contaminated with bone-seeking radionuclides (e.g. contamination of the Techa River), these can be ingested by people of different ages (from newborns to adults) [1–3, 17]. That is why it is important to develop phantoms for various age groups. We have already created phantoms representing skeletons of a newborn [18] and a 1-year-old child [19] within the framework of the SPSD approach.

The study was aimed to develop a computational phantom representing a 5-year-old child's skeleton for estimation of doses to RBM from the beta emitting radionuclides incorporated in the bone. This study represents the next stage of work on the development of a set of reference man computational phantoms for various age groups.

METHODS

Phantoms were created using the original SPSD method previously used to create phantoms representing a newborn [17] and a 1-year-old child [18].

Only the bone fragments containing RBM, i.e. skeletal sites with active hematopoiesis (hematopoietic sites), determined in accordance with the published data on the RBM distribution across the skeleton, were modeled within the framework of the SPSD methodology [20].

The SPSD phantom of the skeletal hematopoietic sites consists of a set of smaller phantoms, the Bone Phantom Segments (BPS) of a simple geometric shape with homogenous bone tissue microarchitecture and cortical layer thickness, describing distinct skeletal bone sites. Such segmentation simplifies the modeling process and enables estimation of the bone microarchitecture heterogeneity within a single hematopoietic site. BPS parameters are based on the published data. The segmentation process details are provided in the earlier reports [13, 21].

Parameters of phantoms included the mineralized bone tissue and bone marrow (simulated media) chemical composition and density, along with the geometry of the source and target tissues comprised in the modeled bone fragment.

Chemical composition and density of the simulated media determined based on the published data were used in all phantoms representing a 5-year-old child [22, 23].

To describe relative position and geometry of tissues inside the bone, we assessed linear dimensions, cortical layer thickness (*Ct. Th.*), and microarchitecture characteristics for each modeled bone site.

To assess morphometric parameters of the phantoms representing a 5-year-old child, we reviewed articles published in peer-reviewed journals, atlases, manuals, monographs, and dissertations. We also reviewed digital resources containing collections of x-ray images. To perform analysis, we collected the measurement results of individuals/samples that were considered to be healthy by the authors and had no disorders resulting in bone deformities. Ethnicity: Caucasians and Mongoloids, since these groups are typical of the Urals region. The subjects' age was 3–7 years.

In this study, the following bone microarchitecture characteristics were assessed based on the published data: trabecular thickness (*Tb. Th.*), trabecular separation (*Tb. Sp.*), bone fraction in the spongiosa volume (*BV/TV*). We considered the measurement data of skeletal bones obtained using various techniques: micrometers, osteometric board, ultrasound and radiography, as well as computed tomography (CT). Histomorphometry and micro-CT data were used to estimate the trabecular bone parameters (*Tb. Th.*, *Tb. Sp.*, *BV/TV*) and the cortical layer thickness.

Average estimates of bone characteristics were taken as computational phantom parameters. When the published data on individual measurements were available, we combined these data to calculate the means and standard deviations (SD). When the measurement results of groups of people were averaged, a weighting factor (W_N) for each group considering the number of subjects (N) was introduced: $W_N = 1$, when $N \geq 25$; $W_N = N/25$, when $N < 25$. Methods to select and assess the published data were previously discussed in detail in [24–26].

A voxel BPS was constructed for each segment using the original Trabecula software [27]. The BPS voxels imitated either mineralized bone, or bone marrow (BM), depending on the voxel center position in the phantom.

Trabecular bone (TB) and cortical bone (CB) were considered as source tissues, while bone marrow (BM) was considered as target tissue. BM was evenly distributed across the trabeculae in the BPS. Voxel size selected individually for each phantom did not exceed 70% of trabecular thickness and varied between 50–200 μm in the generated phantoms [27, 28]. The source and target tissue volumes were automatically calculated in the Trabecula software for each BPS.

Hematopoietic sites of a 5-year-old child, segmentation and BPS generated are provided in Fig. (exemplified by the scapula).

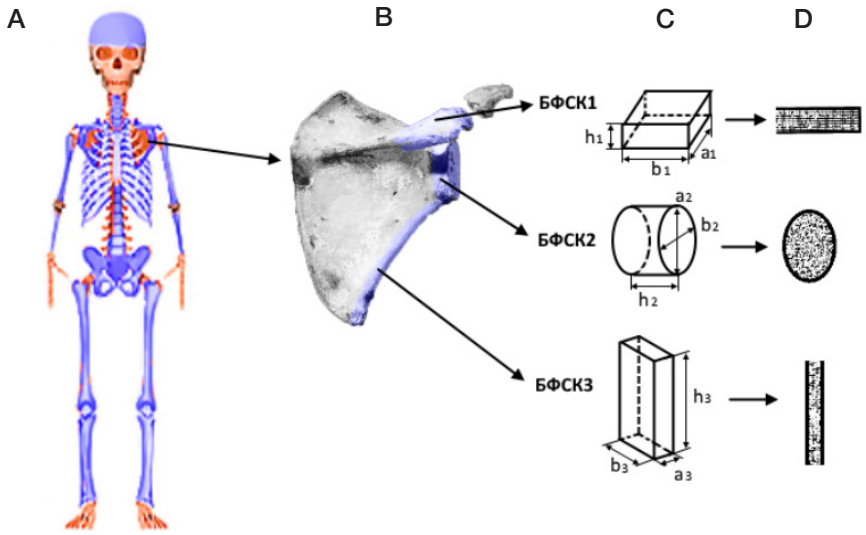

Fig. Segmentation of the skeletal hematopoietic site of a 5-year-old child exemplified by the scapula. **A**. Skeleton of a 5-year-old child (skeletal sites with active hematopoiesis are highlighted in *blue*). **B**. Scapula. **C**. Scheme of bone division into BPS and BPS dimensions. **G**. BPS of the scapula — voxel representation, cross section (voxels simulating bone tissue are highlighted in *black*, those simulating RBM are highlighted in *white*)

To simulate population variability in the size and micro-structure characteristics for each BPS, 12 Supplementary Phantom Segments (SPS) were created with the bone micro- and macro-structure parameters randomly selected within the range of their individual variability (within the limits of minimum and maximum measured values).

RESULTS

The main hematopoietic sites of the 5-year-old child's skeleton and the mass fraction of RBM in these sites were determined based on the MRI data (Table 1) [20].

The skeleton of a 5-year-old child includes 14 hematopoietic sites for simulation (Table 1). The share of RBM in these sites in the total skeletal RBM content varies from 0.9% to 18.1%. Distribution of RBM within each hematopoietic site was also determined based on the published MRI data [29–33].

Chemical composition of the simulated media was selected based on ICRP data for adults (Table 2) [22].

The mineralized bone tissue density estimated based on the cortical bone density measured in 5-year-old children was 1.80 g/cm^3 [23]. The RBM density was taken equal to the water density (1 g/cm^3) [22].

The spongiosa parameters were assessed based on the published data; the analysis and calculation of average population value of the spongiosa parameters were described in detail in [26]. The BPS micro-architecture parameter values for a 1-year-old child are provided in Table 3.

The linear dimensions and thickness of the cortical layer assumed/used for the BPS representing a 5-year-old child are provided in Table 4.

The phantom representing skeletal hematopoietic sites of a 5-year-old child consists of 43 BPS (Table 4). A different number of BPS was used to describe these, depending on the shape of the simulated hematopoietic site: 1 (ribs) to 9 (sacrum).

As in phantoms representing skeletons of people of other ages, most BPS of a 5-year-old child are cylinders and rectangular parallelepipeds; BSP size is within 3–75 mm. The minimum *Ct. Th*. value was reported for the sternal BPS (0.1 mm), while the maximum value was reported for the femoral diaphysis (3.7 mm). The spongiosa parameters varied greatly. The *BV/TV* ratio of BPS was 13–52%, *Tb. Th*. was 0.09–0.29 mm, and *Tb. Sp.* was 0.48–0.98 mm (Table 3).

The average individual variability of the BPS dimensional parameters was 14%; the highest variability value was reported for the ribs (35%), while the lowest value was reported for the

Table 1. Mass fraction of RBM (% of the total mass of RBM in the skeleton) in the main hematopoietic sites of the 5-year-old child's skeleton

№	Hematopoietic site	RBM mass fraction, %
1	Femur	13.5
2	Humerus	4.8
3	Sacrum	5.7
4	Tibia bones	9.3
5	Pelvic bones	13.5
6	Skull	18.0
7	Clavicle	0.9
8	Scapula	2.8
9	Sternum	1.7
10	Ribs	9.0
11	Radius and ulna	2.1
12	Cervical vertebrae	2.3
13	Thoracic vertebrae	9.2
14	Lumbar vertebrae	7.0

Table 2. Chemical composition of simulated media adopted for all BPS

Chemical composition, rel. units		
Chemical element	Bone	Active marrow
H	0.035	0.105
C	0.16	0.414
N	0.042	0.034
O	0.445	0.439
Na	0.003	0.001
Mg	0.002	0.002
P	0.095	0.002
S	0.003	0.002
Ca	0.215	–

distal part of the humerus (3%). The average cortical layer thickness was 26%, with the maximum value of 35% reported for the sacral segments and the minimum value of 7% reported for bodies of the cervical vertebrae. The average variability of spongiosa parameters was 18%, with the minimum value of 2% and maximum value of 70%.

Variability values were used for SPS modeling. SPS volume varies greatly, it can differ from the BPS volume by a factor of three, both upwards and downwards. In our future studies, DFs will be calculated for both BPS and SPS. Standard deviation of DFs calculated for SPS from DFs calculated for BPS will characterize the DF population variability.

DISCUSSION

Comparison of the modeling outcome with the masses of real bones was performed for the newborn in order to confirm the methodological approach accuracy. We have found no masses or volumes of the wet bones of 5-year-old children, that is why we cannot compare the modeling outcome with the real bones. The existing computational phantoms obtained by scanning autopsy material are non-parametric, that is why it is impossible to compare parameters of these phantoms with the SPSD phantom parameters. For most bones, it is also impossible to compare the characteristics of phantoms obtained as a result of their generation (masses of simulated media) with the published phantom masses, since only skeletal sites with active hematopoiesis are modeled within the framework of the SPSD approach, not the entire skeleton. The SPSD phantom masses (sums of masses of all segments comprised in the phantom) were compared with the published data for the bones, which were modeled as a whole: pelvic bones and the clavicle of a 5-year-old child [7, 12]. The comparison showed that the difference between the phantom masses reported in the published papers and the SPSD phantom masses did not exceed 20%.

It makes sense to assess age-related changes in the characteristics of phantoms representing a newborn, 1-year-old and 5-year-old children. The phantom representing a skeleton of a 5-year-old child consists of a larger number of BPS than the phantoms representing skeletons of younger children. This is associated with the processes underlying cartilage mineralization that are intense within the first five years of life; in particular, vertebral processes and the sternum have undergone significant mineralization by the age of 5. Furthermore, the process of the RBM substitution with adipose tissue in the tubular bone diaphysis is not over yet in children of this age, that is why BPS were modeled for these sites. Significant changes in the RBM distribution across the skeleton occur by the age of 5. Thus, children of this age have a significantly lower mass fraction of RBM in the skull compared to 1-year-old children (28.7% vs. 18.1%), furthermore, fraction of RBM in other skeletal segments is increased. The BPS micro-structure parameters show little changes. The cortical layer thickness

Table 3. Spongiosa parameters taken for BPS of a 5-year-old-child [11, 34–55] (coefficient of variation (CV) is given in parentheses, %)

Hematopoietic site	*BV*/*TV*, %	*Tb. Th*, mm	*Tb. Sp*, mm
Femur (proximal part)	35 (6)	0.24 (22)	0.77 (70)
Femur (central and distal parts)	26 (6)		
Humerus	22 (7)	0.21 (13)	0.58 (47)
Ribs	20 (6)	0.23 (34)	0.51 (14)
Tibia bones*	25 (3)	0.13 (13)	0.74 (11)
Pelvic bones	25 (2)	0.15 (11)	0.48 (23)
Skull*	52 (5)	0.29 (31)	0.57 (35)
Clavicle*	15 (3) 29 (9)	0.2 (32) 0.15 (13)	0.80 (25)
Radius and ulna	16 (5)	0.16 (13)	0.77 (16)
Scapula*	22 (8)	0.24 (42)	0.96 (23)
Sternum*	15 (27)	0.14 (33)	1.0 (6)
Cervical vertebrae	21 (5)	0.14 (14)	0.60 (20)
Thoracic vertebrae + lumbar vertebrae + sacrum	13 (4)	0.09 (40)	0.60 (20)

Note: * — spongiosa parameters were calculated based on the measurement results of similar bones or based on the data for other age groups; the calculation method was reported previously in [25].

Table 4. Linear dimensions and thickness of the cortical layer taken for the BPS representing a 5-year-old child

Hematopoietic site	Segment	Shape[1]	Phantom parameters, mm (CV is given in parentheses, %)[2]						Data sources
			h	*a*	*b*	*c*	*d*	*Ct.Th.*	
Femur	Diaphysis[4]	c	30	17 (6)	17 (6)			3.7 (8)	[56–64]
	Proximal end (upper part)	c	25 (4)	23 (30)	23 (30)			1.3 (14)	
	Proximal end (lower part)	c	25 (4)	23 (30)	23 (30)			1.2 (14)	
	Distal end	dc	49 (4)	68 (6)	25 (7)	17 (6)	17 (6)	1.1 (7)	
Humerus	Diaphysis[4]	c	30	15 (3)	15 (3)			2.5 (20)	[56–59,65]
	Proximal end	dc	20 (4)	32 (5)	32 (5)	15 (5)	15 (5)	0.9 (18)	
	Distal end	dc	27 (4)	46 (7)	15 (3)	15 (3)	15 (3)	0.8 (19)	
Ribs	Ribs[4]	p	9.4 (32)	30	4.4 (35)			0.5 (33)	[66–68]
Sacrum	Body of the 1st vertebra	p	17 (20)	75 (20)	21 (6)			0.7 (35)	[69–72]
	Body of the 2nd vertebra	p	16 (20)	60 (20)	15 (10)			0.7 (35)	
	Body of the 3rd vertebra	p	14 (20)	52 (20)	11 (10)			0.7 (35)	
	Body of the 4th vertebra	p	10 (20)	45 (20)	6.4 (9)			0.7 (35)	
	Body of the 5th vertebra	p	10 (20)	22 (20)	6.4 (9)			0.7 (35)	
Tibia bones	Fibula[4]	c	30	8.1 (6)	8.1 (6)			1.5 (20)	[56, 73, 74]
	Tibia diaphysis[4]	c	30	15(4)	15 (4)			2.9 (17)	[55, 56, 60, 75–77]
	Tibia proximal end б. б.	dc	34 (5)	55 (6)	22 (20)	15 (4)	15 (4)	0.7 (18)	
	Tibia distal end	dc	34 (5)	24 (22)	24 (23)	15 (4)	15 (4)	0.7 (18)	
Pelvic bones	Ilium part 1	p	7.9 (13)	30	30			"1.6 (33) 0.8 (20)3"	[78–85]
	Ilium part 2	p	7.9 (13)	30	30			0.8 (20)	
	Acetabular part of the ilium	dc	20 (8)	35 (10)	16 (30)	34 (30)	27 (30)	0.8 (20)	
	Acetabular part of the pubis	dc	7.3 (15)	22 (20)	18 (20)	13 (11)	8.8 (20)	0.5 (30)	
	Pubis bone (superior ramus)	c	29 (15)	13 (11)	8.8 (20)			0.5 (30)	
	Pubis bone (inferior ramus)	c	19 (15)	8.8 (20)	8.8 (20)			0.5 (30)	
	Acetabular part of the ischium	p	21 (15)	21 (15)	27 (15)	21 (15)		0.5 (30)	
	Ischial tuberosity	c	25 (15)	18 (15)	14 (15)			0.5 (30)	
	Inferior ramus of the ischium	c	19 (15)	8.8 (20)	8.8 (20)			0.5 (30)	
Skull	Flat bones[4]	p	4.2 (26)	30	30			1.1 (26)	[86–88]
Clavicle	Body[4]	c	30	8.7 (9)	6.8 (10)			1.1 (9)	[89–92]
	Sternal end	dc	12 (13)	18 (10)	16 (9)	8.7 (9)	6.8 (10)	0.5 (10)	
	Acromial end	dc	12 (13)	15 (11)	8.7 (18)	8.7 (9)	6.8 (10)	0.5 (10)	
Radius and ulna	Diaphysis[4]	c	30	8.3 (25)	8.3 (17)			1.5 (12)	[56, 58, 73]
	End	dc	26 (5)	13 (6)	8.3 (5)	8.3 (5)	8.3 (5)	0.5 (29)	
Scapula	Glenoid	c	12 (8)	25 (11)	18 (7)			0.9 (28)	[93–96]
	Acromion	p	7.6 (18)	20 (12)	16 (12)			0.8 (13)	
	Lateral border	p	30	3.2 (6)	10 (12)			0.8 (13)	
Sternum	Sternum	p	6.9 (13)	30	30			0.1 (19)	[37, 97, 98]
Cervical vertebrae	Vertebral body	c	7.3 (8)	11.3 (12)	18.1 (12)			0.2 (7)	[51,99–102]
Thoracic vertebrae	Vertebral body	c	12 (17)	17 (17)	21 (20)			0.2 (25)	[51,100–103,104]
	Transverse process	p	7.3 (19)	11 (19)	5.3 (19)			0.2 (25)	
	Spinous process	p	5.9 (21)	17 (21)	3 (21)			0.2 (25)	
Lumbar vertebrae	Vertebral body	c	16 (11)	23 (12)	34 (13)			0.2 (25)	[51,71,100–103, 105]
	Transverse process	p	6.4 (13)	12 (12)	5 (12)			0.2 (25)	
	Spinous process	p	15 (20)	13 (20)	5 (20)			0.2 (25)	

Note: [1] — phantom shape was designated as follows: c — cylinder, dc — deformed cylinder, *p* — rectangular parallelepiped, e — ellipsoid; 2 — BPS dimensions were designated as follows: *h* — height; *a* — major axis (c), major axis for a larger base (dc) or side a (p); *b* — minor axis (c), minor axis for a large base (dc) or side b (p); *c* — major axis for a small base (dc); *d* — minor axis for a small base (dc); [3] — cortical layer thickness was considered to be different for the inner (medial) and outer (gluteal) surfaces of this segment of the ilium; [4] — BPS imitated only a part of the simulated bone segment, when the bone segment dimensions significantly exceeded 30 mm, since in such cases it makes no sense to simulate the entire bone fragment in terms of dosimetry [14, 21].

Table 5. Comparison of BPS volumes of 1-year-old and 5-year-old children

BPS	Simulated medium	Modeled structure volume, cm^3		
		1 year	5 years	1 year / 5 years
Distal end of the femur	BM	6.53	22.9	3.51
	TB	1.88	7.56	4.02
	CB	1.41	5.21	3.7
	Entire BPS	9.82	35.67	3.63
Sternal end of the clavicle	BM	0.35	0.89	2.54
	TB	0.14	0.36	2.57
	CB	0.09	0.22	2.44
	Entire BPS	0.58	1.47	2.53
Body of the lumbar vertebra	BM	1.32	8.51	6.45
	TB	0.2	1.34	6.7
	CB	–	0.3	–
	Entire BPS	1.52	10.15	6.68
Body of the cervical vertebra	BM	0.45	0.89	1.98
	TB	0.11	0.24	2.18
	CB	–	0.05	–
	Entire BPS	0.56	1.18	2.11

significantly increases during this period; all the modeled skeletal segments become covered with the cortical layer by the age of 5, in contrast to phantoms representing a newborn and a 1-year-old child. In the period from the age of one to five years, the size of all parts of the skeleton increases significantly. Comparison of the volumes of phantoms representing skeletal segments of 1-year-old and 5-year-old children exemplified by the distal part of the femur, clavicle, bodies of the cervical and lumbar vertebrae is provided in Table 5.

As shown in Table 5, the volumes of simulated media of a 5-year-old child largely exceed those of the 1-year-old child. The increase in the source tissue volume for this period is 3.26-fold and 2.78-fold for TB and CB, respectively. The CB volume increase is 3.03-fold. The total BPS volume of a 5-year-old child is on average 2.8 times larger than the volume of the phantom representing a 1-year-old child.

We expect that such age-related changes will have a significant impact on the average DF of the skeleton and, therefore, on the dose rate. The increase in the BPS linear dimensions can have the greatest effect on the DF for strontium incorporated in the trabecular bone. Previous studies have shown that the larger the BPS size, the greater the chance is of absorbing energy from the incorporated radionuclide within the phantom, not outside it [15, 16]. The opposite pattern is typical of strontium in the cortical bone: the larger the phantom size, the lower the likelihood of energy transfer from the source incorporated on the outer cortical layer to the target (RBM) is. Thus, when the BPS size increases, one can expect the increase in DF for ^{89,90}Sr in the trabecular bone and decrease in DF for Sr in the cortical bone.

The phantom parameters provided (Tables 3, 4) can be integrated in the Trabecula software to generate voxel phantoms. Modeling of radiation transport using voxel phantoms will make it possible to assess DFs for bone-seeking beta emitters, thereby allowing one to determine the RBM absorbed dose rate.

CONCLUSIONS

The study resulted in the development of computational phantoms representing the main skeletal sites of a 5-year-old child with active hematopoiesis. These phantoms were developed using the same method, as for the newborn and 1-year-old child. The phantoms modeled imitate bone tissue structure, while the sets of phantoms simulate population variability in the size of structures of distinct bones. The provided phantom representing a 5-year-old child will be used to calculate DFs for ^{89,90}Sr, which, in turn, are essential for estimates of adjusted coefficients linking individual radionuclide uptake and dose to RBM, which will help to improve dose estimates for the Urals region residents. As the way forward, we also plan to create SPSD phantoms representing skeletons of people of other age groups: 10 year-olds, 15-year-olds and adults. SPSD phantoms can be used for the incorporated bone-seeking beta emitter dosimetry in the population, in case of radionuclide contamination of the environment, as well as for dosimetry from other bone-seeking beta emitters, including those used in radionuclide therapy, such as ^{89}Sr, ^{32}P, ^{186}Re, ^{188}Re, ^{117}mSn.

References

1. Degteva MO, Shagina NB, Vorobiova MI, Shishkina EA, Tolstykh EI, Akleyev AV. Contemporary Understanding of Radioactive Contamination of the Techa River in 1949–1956. Radiats Biol Radioecol. 2016; 56 (5): 523–34. PMID: 30703313.
2. Krestinina LY, Epifanova SB, Silkin SS, Mikryukova LD, Degteva MO, Shagina NB, Akleyev AV. Chronic low-dose exposure in the Techa River Cohort: risk of mortality from circulatory diseases. Radiat Environ Biophys. 2013; 52 (1): 47–57. DOI: 10.1007/s00411-012-0438-5.
3. Akleev AV. Hronicheskij luchevoj sindrom u zhitelej pribrezhnyh sel reki Techa. Cheljabinsk: Kniga, 2012; p. 464. Russian.
4. Preston DL, Sokolnikov ME, Krestinina LY, Stram DO. Estimates

of radiation effects on cancer risks in the Mayak Worker, Techa River and Atomic Bomb Survivor Studies. Radiat Prot Dosimetry. 2017; 173 (1–3): 26–31. DOI: 10.1093/rpd/ncw316.
5. Degteva MO, Napier BA, Tolstykh EI, et al. Enhancements in the Techa River dosimetry system: TRDS-2016D Code for reconstruction of deterministic estimates of dose from environmental exposures. Health Phys. 2019; 117 (4): 378–87. DOI:10.1097/HP.0000000000001067.
6. Spiers FW, Beddoe AH, Whitwell JR. Mean skeletal dose factors for beta-particle emitters in human bone. Part I: volume-seeking radionuclides. The British journal of radiology. 1978; 51 (608): 622–7.
7. O'Reilly SE, DeWeese LS, Maynard MR, Rajon DA, Wayson MB, Marshall EL, et al. An 13 image-based skeletal dosimetry model for the ICRP reference adult female-internal electron 14 sources. Phys Med Biol. 2016; 61 (24): 8794–824.
8. Xu XG, Chao TC, Bozkurt A. VIP-Man: an image-based whole-body adult male model constructed from color photographs of the Visible Human Project for multi-particle Monte Carlo calculations. Health Phys. 2000; 78 (5): 476–86. DOI: 10.1097/00004032-200005000-00003. PMID: 10772019.
9. Shah AP, Bolch WE, Rajon DA, Patton PW, Jokisch DW. A paired-image radiation transport model for skeletal dosimetry. J Nucl Med. 2005; 46 (2): 344–53. PMID: 15695796.
10. Pafundi D. Image-based skeletal tissues and electron dosimetry models for the ICRP reference pediatric age series [dissertation]. Gainesville: University of Florida, 2009.
11. Hough M, Johnson P, Rajon D, Jokisch D, Lee C, Bolch W. An image-based skeletal dosimetry model for the ICRP reference adult male–internal electron sources. Phys Med Biol. 2011; 56 (8): 2309–46. DOI: 10.1088/0031-9155/56/8/001.
12. Bolch WE, Eckerman K, Endo A, et al. ICRP Publication 143: Paediatric Reference Computational Phantoms. Ann ICRP. 2020; 49 (1): 5–297. DOI: 10.1177/0146645320915031.
13. Degteva MO, Tolstykh EI, Shishkina EA, Sharagin PA, Zalyapin VI, Volchkova AY, et al. Stochastic parametric skeletal dosimetry model for humans: General approach and application to active marrow exposure from bone-seeking beta-particle emitters. PLoS ONE. 2021; 16 (10): e0257605. DOI: 10.1371/journal.pone.0257605.
14. Degteva MO, Shishkina EA, Tolstykh EI, Zalyapin VI, Sharagin PA, Smith MA, et al. Methodological approach to development of dosimetric models of the human skeleton for beta-emitting radionuclides. Radiation Hygiene. 2019; 12 (2): 66–75. DOI: 10.21514/1998-426X-2019-12-2-66-75. Russian.
15. Volchkova AYu, Sharagin PA, Shishkina EA. Internal bone marrow dosimetry: the effect of the exposure due to 90Sr incorporated in the adjacent bone segments. Bulletin of the South Ural State University. Ser. Mathematical Modelling, Programming & Computer Software. 2022; 15 (4): 44–58. DOI: 10.14529/mmp220404.
16. Shishkina EA, Sharagin PA, Volchkova AYu. Analytical description of dose forming in bone marrow from 90Sr in calcified tissues. Issues of Radiation Safety. 2021; 3: 72–82. Russian.
17. Silkin SS, Krestinina LYu, Startsev VN, Akleev AV. Ural cohort of emergency-irradiated population. Extreme medicine. 2019; 21 (3): 393–402. Russian.
18. Sharagin PA, Shishkina EA, Tolstykh EI. Computational phantom for red bone marrow dosimetry from incorporated beta emitters in a newborn baby. Extreme Medicine. 2022; 4: 74–82. DOI: 10.47183/mes.2022.045. Russian.
19. Sharagin PA, Shishkina EA, Tolstykh EI. Computational red bone marrow dosimetry phantom of a one-year-old child enabling assessment of exposure due to incorporated beta emitters. Extreme Medicine. 2023; 3: 44–55. DOI: 10.47183/mes.2023.030. Russian.
20. Cristy M. Active bone marrow distribution as a function of age in humans. Phys Med Biol. 1981; 26 (3): 389–400.
21. Sharagin PA, Shishkina EA, Tolstykh EI, Volchkova AYu, Smith MA, Degteva MO. Segmentation of hematopoietic sites of human skeleton for calculations of dose to active marrow exposed to bone-seeking radionuclides. RAD Conference Proceedings. 2018; 3: 154–8. DOI:10.21175/RadProc.2018.33.
22. Valentin J. Basic anatomical and physiological data for use in radiological protection: reference values. Annals of the ICRP. Annals of the ICRP. 2002; 32 (3–4): 1–277.
23. Woodard HQ and White DR. The composition of body tissues. Br. J. Ru&ol. 1986; 59: 1209–18.
24. Sharagin PA, Tolstykh EI, Shishkina EA, Degteva MO. Dosimetric modeling of bone for bone-seeking beta-emitting radionuclides: size parameters and segmentation. In: Proceedings of the contemporary issues of radiobiology — 2021 International Scientific Conference; 2021 Sept 23–24; Gomel, Belarus. 2021; p. 200–4. Russian.
25. Tolstykh EI, Sharagin PA, Shishkina EA, Degteva MO. Dosimetric modeling of red bone marrow exposure from 89,90Sr: resolving age-dependent trabecular bone parameters. In: Proceedings of the contemporary issues of radiobiology — 2021 International Scientific Conference; 2021 Sept 23–24; Gomel, Belarus. 2021; p. 176–9. Russian.
26. Tolstykh EI, Sharagin PA, Shishkina EA, Volchkova AY, Degteva MO. Anatomical and morphological basis for dosimetric modeling of the human trabecular bone using a stochastic parametric approach. Clinical Bulletin of the Burnazyan State Medical Center. 2022; 3: 25–40. Russian.
27. Shishkina EA, Timofeev YS, Volchkova AY, Sharagin PA, Zalyapin VI, Degteva MO, et al. Trabecula: a random generator of computational phantoms for bone marrow dosimetry. Health Phys. 2020; 118 (1): 53–9. DOI: 10.1097/HP.0000000000001127.
28. Zalyapin VI, Timofeev YuS, Shishkina EA. A parametric stochastic model of bone geometry. Bulletin of Southern Urals State University, Issue «Mathematical Modelling. Programming & Computer Software» (SUSU MMCS). 2018; 11 (2): 44–57. DOI: 10.14529/mmp180204.
29. Robinson RA. Chemical analysis and electron microscopy of bone. In: Rodahl K, Nicholson JT, Brown EM, editors. Bone as a tissue. New York: McGraw-Hill, 1960; p. 186–250.
30. Vogler JB 3rd, Murphy WA. Bone marrow imaging. Radiology. 1988; 168 (3): 679–93.
31. Vande Berg BC, Malghem J, Lecouvet FE, Maldague B. Magnetic resonance imaging of the normal bone marrow. Skeletal Radiology. 1998; 27: 471–83.
32. Vande Berg BC, Malghem J, Lecouvet FE, Maldague B. Magnetic resonance imaging of normal bone marrow. Eur Radiol. 1998; 8 (8): 1327–34.
33. Taccone A, Oddone M, Dell'Acqua AD, Occhi M, Ciccone MA. MRI «road-map» of normal age-related bone marrow. II. Thorax, pelvis and extremities. Pediatr Radiol. 1995; 25 (8): 596–606. PubMed PMID: 8570312.
34. Taccone A, Oddone M, Occhi M, Dell'Acqua AD, Ciccone MA. MRI «road-map» of normal age-related bone marrow. I. Cranial bone and spine. Pediatr Radiol. 1995; 25 (8): 588–95. PubMed PMID: 8570311.
35. Milovanovic P, Djonic D, Hahn M, Amling M, Busse B, Djuric M. Region-dependent patterns of trabecular bone growth in the human proximal femur: A study of 3D bone microarchitecture from early postnatal to late childhood period. Am J Phys Anthropol. 2017; 164 (2): 281–91. DOI: 10.1002/ajpa.23268.
36. Ryan TM, Krovitz GE. Trabecular bone ontogeny in the human proximal femur. J Hum Evol. 2006; 51 (6): 591–602.
37. Cunningham C, Scheuer L, Black S. Developmental Juvenile Osteology. 2rd ed. Elsevier Academic Press, 2016; p. 630.
38. Ryan TM, Raichlen DA, Gosman JH. Structural and mechanical changes in trabecular bone during early development in the human femur and humerus. Chapter 12. In: Percival CJ, Richtsmeier JT, editors. Building Bones: Bone Formation and Development in Anthropology. Cambridge University Press, 2017; p. 281–302.
39. Glorieux FH, Travers R, Taylor A, Bowen JR, Rauch F, Norman M, et al. Normative data for iliac bone histomorphometry in growing children. Bone. 2000; 26 (2): 103–9.
40. Volpato V. Bone endostructure morphogenesis of the human ilium. C. R. Palevol 7. 2008; 463–71. DOI: 10.1016/j.crpv.2008.06.001.
41. Rodriguez-Florez N, Ibrahim A, Hutchinson JC, Borghi A, James G, Arthurs OJ, et al. Cranial bone structure in children with sagittal craniosynostosis: Relationship with surgical outcomes. J Plast Reconstr Aesthet Surg. 2017; 70 (11): 1589–97. DOI: 10.1016/j.bjps.2017.06.017.

42. Gao S, Ren L, Qui R, Wu Z, Li C, Li J. Electron absorbed fractions in an image-based microscopic skeletal dosimetry model of chinese adult male. Radiat Prot Dosimetry. 2017; 175 (4): 450–9.
43. Pafundi D. Image-based skeletal tissues and electron dosimetry models for the ICRP reference pediatric age series [dissertation]. Gainesville: University of Florida, 2009.
44. Milenković P. Age Estimation Based on Analyses of Sternal End of Clavicle and the First Costal Cartilage Doctoral Dissertation [dissertation]. Belgrade: University Of Belgrade School of Medicine, 2013.
45. Kirmani S, Christen D, van Lenthe GH, Fischer PR, Bouxsein ML, McCready LK, et al. Bone structure at the distal radius during adolescent growth. J Bone Miner Res. 2009; 24 (6): 1033–42. DOI: 10.1359/jbmr.081255.
46. Mitchell DM, Caksa S, Yuan A, Bouxsein ML, Misra M, Burnett-Bowie SM. Trabecular bone morphology correlates with skeletal maturity and body composition in healthy adolescent girls. J Clin Endocrinol Metab. 2018; 103 (1): 336–45. DOI: 10.1210/jc.2017-01785.
47. Li X, Williams P, Curry EJ, Choi D, Craig EV, Warren RF, et al. Trabecular bone microarchitecture and characteristics in different regions of the glenoid. Orthopedics. 2015; 38 (3): 163–8.
48. Knowles NK, G Langohr GD, Faieghi M, Nelson A, Ferreira LM. Development of a validated glenoid trabecular density-modulus relationship. J Mech Behav Biomed Mater. 2019; 90: 140–5. DOI: 10.1016/j.jmbbm.2018.10.013.
49. Jun BJ, Vasanji A, Ricchetti ET, Rodriguez E, Subhas N, Li ZM, Iannotti JP. Quantification of regional variations in glenoid trabecular bone architecture and mineralization using clinical computed tomography images. J Orthop Res. 2018; 36 (1): 85–96. DOI: 10.1002/jor.23620.
50. Frich LH, Odgaard A, Dalstra M. Glenoid bone architecture J Shoulder Elbow Surg. 1998; 7 (4): 356–61.
51. Kneissel M, Roschger P, Steiner W, et al. Cancellous bone structure in the growing and aging lumbar spine in a historic Nubian population. Calcif Tissue Int. 1997; 61 (2): 95–100. DOI: 10.1007/s002239900302.
52. Arbabi A. A quantitative analysis of the structure of human sternum. J Med Phys. 2009; 34 (2): 80–6.
53. Bartl R, Frisch B. Biopsy of bone in internal medicine — an atlas and sourcebook. Dordrecht: Kluwer Academic Publishers, 1993; p. 250.
54. Baur-Melnyk A. Magnetic Resonance Imaging of the Bone Marrow. Springer Science & Business Media, 2012; p. 371.
55. Florence JL. Linear and cortical bone dimensions as indicators of health status in subadults from the Milwaukee County Poor Farm Cemetery. M. A.: University of Colorado at Denver, 2007.
56. Maresh MM. Measurements from roentgenograms. In: McCammon RW, editor. Human Growth and Development. Springfield, IL: Charles C. Thomas, 1970; p. 157–200.
57. Singh SP, Malhotra P, Sidhu LS, Singh PP. Skeletal frame size of spitian children. Journal of Human Ecology. 2007; 21 (3): 227–30.
58. Zivicnjak M, Smolej Narancić N, Szirovicza L, Franke D, Hrenović J, Bisof V, et al. Gender-specific growth patterns of transversal body dimensions in Croatian children and youth (2 to 18 years of age). Coll Antropol. 2008; 32 (2): 419–31. PubMed PMID: 18756891.
59. Svadovskij BS. Vozrastnaja perestrojka kostnoj tkani. O roste i razvitii diafizov plechevoj i bedrennoj kostej. M.: Izd-vo akad. ped. nauk RSFSR, 1961; p. 110. Russian.
60. Miles AEW. Growth Curves of Immature Bones from a Scottish Island Population of Sixteenth to mid-Nineteenth Century: Limb-bone Diaphyses and Some Bones of the Hand and Foot. International Journal of Osteoarcheology. 1994; 4: 121–36.
61. Dhavale N, Halcrow SE, Buckley HR, Tayles N, Domett KM, Gray AR. Linear and appositional growth in infants and children from the prehistoric settlement of Ban Non Wat, Northeast Thailand: Evaluating biological responses to agricultural intensification in Southeast Asia, Journal of Archaeological Science: Reports. 2017; 11: 435–46. ISSN 2352-409.
62. Djurić M, Milovanović P, Djonić D, Minić A, Hahn M. Morphological characteristics of the developing proximal femur: a biomechanical perspective. Srp Arh Celok Lek. 2012; 140 (11–12): 738–45. PubMed PMID: 23350248.
63. Gosman JH, Ketcham RA. Patterns in ontogeny of human trabecular bone from SunWatch Village in the Prehistoric Ohio Valley: general features of microarchitectural change. Am J Phys Anthropol. 2009; 138 (3): 318–32. DOI: 10.1002/ajpa.20931. PubMed PMID: 18785633.
64. Petit MA, McKay HA, MacKelvie KJ, Heinonen A, Khan KM, Beck TJ. A randomized school-based jumping intervention confers site and maturity-specific benefits on bone structural properties in girls: a hip structural analysis study. J Bone Miner Res. 2002; 17 (3): 363–72. PubMed PMID: 11874228.
65. Danforth ME, Wrobel GD, Armstrong CW, Swanson D. Juvenile age estimation using diaphyseal long bone lengths among ancient Maya populations. Latin American Antiquity. 2017; 20 (1): 3–13.
66. Byers S, Moore AJ, Byard RW, Fazzalari NL. Quantitative histomorphometric analysis of the human growth plate from birth to adolescence. Bone. 2000; 27 (4): 495–501.
67. Beresheim AC, Pfeiffer S, Grynpas M. Ontogenetic changes to bone microstructure in an archaeologically derived sample of human ribs. J Anat. 2019; DOI: 10.1111/joa.13116.
68. Pfeiffer S. Cortical Bone Histology in Juveniles. Available from: https://www.researchgate.net/publication/303179375_Cortical_bone_histology_in_Juveniles.
69. Hresko AM, Hinchcliff EM, Deckey DG, Hresko MT. Developmental sacral morphology: MR study from infancy to skeletal maturity. Eur Spine J. 2020; 29 (5): 1141–6. DOI: 10.1007/s00586-020-06350-6.
70. Kuznecov LE. Perelomy taza u detej (morfologija, biomehanika, diagnostika). M.: Folium, 1994; p. 192. Russian.
71. Mavrych V, Bolgova O, Ganguly P and Kashchenko S. Age-related changes of lumbar vertebral body morphometry. Austin J Anat. 2014; 1 (3): 7.
72. Sadofeva VI. Normal'naja rentgenoanatomija kostno-sustavnoj sistemy detej. Leningrad: Medicina, 1990; p. 216. Russian.
73. Bernert Zs, Évinger S, Hajdu T. New data on the biological age estimation of children using bone measurements based on historical populations from the Carpathian Basin. Annales Historico-Naturales Musei Nationalis Hungarici. 2007; 99: 199–206.
74. White TD, Black MT, Folkens PA. Human osteology: 3rd ed. Academic Press, 2011; p. 688.
75. Gindhart PS. Growth standards for the tibia and radius in children aged one month through eighteen years. Am J Phys Anthrop. 1973; 39: 41–8.
76. Lopez-Costas O, Rissech C, Trancho G, Turbón D. Postnatal ontogenesis of the tibia. Implications for age and sex estimation. Forensic Sci Int. 2012; 214 (1–3): 207.e1–11. DOI: 10.1016/j.forsciint.2011.07.038. PubMed PMID: 21862250.
77. Suominen PK, Nurmi E, Lauerma K. Intraosseous access in neonates and infants: risk of severe complications — a case report. Acta Anaesthesiol Scand. 2015; 59 (10): 1389–93. DOI: 10.1111/aas.12602. PubMed PMID: 26300243.
78. Blake KAS. An investigation of sex determination from the subadult pelvis: A morphometric analysis [dissertation]. Pittsburgh: University of Pittsburgh, 2011.
79. Cunningham CA, Black SM. Iliac cortical thickness in the neonate — the gradient effect. J Anat. 2009a; 215 (3): 364–70. DOI: 10.1111/j.1469-7580.2009.01112.x.
80. Cunningham CA, Black SM. Anticipating bipedalism: trabecular organization in the newborn ilium. J Anat. 2009b; 214 (6): 817–29. DOI: 10.1111/j.1469-7580.2009.01073.x.
81. Rissech C, Garcıa M, Malgosa A. Sex and age diagnosis by ischium morphometric analysis. Forensic Science International. 2003; 135: 188–96.
82. Rissech C, Malgosa A. Pubis growth study: Applicability in sexual and age diagnostic. Forensic Science International. 2007; 173: 137–45.
83. Corron L, Marchal F, Condemi S, Chaumoître K, Adalian P. A New Approach of Juvenile Age Estimation using Measurements of the Ilium and Multivariate Adaptive Regression Splines (MARS) Models for Better Age Prediction. Forensic Sci. 2017; 62 (1): 18–29. DOI: 10.1111/1556-4029.13224.
84. Parfitt AM, Travers R, Rauch F, Glorieux FH. Structural and cellular changes during bone growth in healthy children. Bone. 2000; 27

(4): 487–94. PMID: 11033443.
85. Schnitzler CM, Mesquita JM, Pettifor JM. Cortical bone development in black and white South African children: iliac crest histomorphometry. Bone. 2009; 44 (4): 603–11. DOI: 10.1016/j.bone.2008.12.009.
86. De Boer HH, Van der Merwe AE, Soerdjbalie-Maikoe VV. Human cranial vault thickness in a contemporary sample of 1097 autopsy cases: relation to body weight, stature, age, sex and ancestry. Int J Legal Med. 2016; 130 (5): 1371–7. DOI: 10.1007/s00414-016-1324-5.
87. Margulies S, Coats B. Experimental injury biomechanics of the pediatric head and brain. Chapter 4. In: Crandall J, Myers B, Meaney D, et al, editors. Pediatric Injury Biomechanics. New York: Springer Science+Business Media, 2013; p. 157–190.
88. Li Z, Park BK, Liu W, Zhang J, Reed MP, Rupp JD, et al. A statistical skull geometry model for children 0–3 years old. PLoS One. 2015; 10 (5). DOI: 10.1371/journal.pone.0127322.
89. Bleuze MM, Wheeler SM, Williams LJ, Dupras TL. Growth of the pectoral girdle in a sample of juveniles from the kellis 2 cemetery, Dakhleh Oasis, Egypt. Am J Hum Biol. 2016; 28 (5): 636–45.
90. McGraw MA, Mehlman CT, Lindsell CJ, Kirby CL. Postnatal growth of the clavicle: birth to eighteen years of age. Journal of Pediatric Orthopedics. 2009; 29: 937.
91. Bernat A, Huysmans T, Van Glabbeek F, Sijbers J, Gielen J, Van Tongel A. The anatomy of the clavicle: a three-dimensional cadaveric study. Clin Anat. 2014; 27 (5): 712–23.
92. Corron L. Juvenile age estimation in physical anthropology: A critical review of existing methods and the application of two standardised methodological approaches. Biological anthropology [dissertation]. Marseille: Aix-Marseille Universite, 2016.
93. Vallois HV. L'omoplate humaine. Bulletin de la Sociétié d'Anthropolgie de Paris. 1946; 7: 16–99.
94. Saunders S, Hoppa R, Southern R. Diaphyseal growth in a nineteenth-century skeletal sample of subadults from St Thomas' Church, Belleville, Ontario. International Journal of Osteoarchaeology. 1993; 3: 265–81.
95. Badr El Dine F, Hassan H. Ontogenetic study of the scapula among some Egyptians: Forensic implications in age and sex estimation using Multidetector Computed Tomography. Egyptian Journal of Forensic Sciences. 2015; 6 (2): 56–77.
96. Rissech C, Black S. Scapular development from neonatal period to skeletal maturity. A preliminary study. Int J Osteoarchaeol. 2007; 17: 451–64.
97. Bayaroğulları H, Yengil E, Davran R, Ağlagül E, Karazincir S, Balcı A. Evaluation of the postnatal development of the sternum and sternal variations using multidetector CT. Diagn Interv Radiol. 2014; 20 (1): 82–9.
98. Riach IC. Ossification in the sternum as a means of assessing skeletal age. J Clin Pathol. 1967; 20 (4): 589–90.
99. Johnson KT, Al-Holou WN, Anderson RC, Wilson TJ, Karnati T, Ibrahim M, et al. Morphometric analysis of the developing pediatric cervical spine. J Neurosurg Pediatr. 2016; 18 (3): 377–89. DOI: 10.3171/2016.3.PEDS1612. PubMed PMID: 27231821.
100. Caldas Md P, Ambrosano GM, Haiter Neto F. New formula to objectively evaluate skeletal maturation using lateral cephalometric radiographs. Braz Oral Res. 2007; 21 (4): 330–5. PubMed PMID: 18060260.
101. Peters JR, Chandrasekaran C, Robinson LF, Servaes SE, Campbell RM Jr, Balasubramanian S. Age- and gender-related changes in pediatric thoracic vertebral morphology. Spine J. 2015; 15 (5): 1000–20. DOI: 10.1016/j.spinee.2015.01.016.
102. Peters JR, Servaes SE, Cahill PJ, Balasubramanian S. Morphology and growth of the pediatric lumbar vertebrae. Spine J. 2021; 21 (4): 682–97. DOI: 10.1016/j.spinee.2020.10.029.
103. Newman SL, Gowland RL. The use of non-adult vertebral dimensions as indicators of growth disruption and non-specific health stress in skeletal populations. American journal of physical anthropology. 2015; 158 (1): 155–64.
104. Comeau A. Age-related changes in geometric characteristics of the pediatric thoracic cage and comparison of thorax shape with a Pediatric CPR Manikin [dissertation]. Philadelphia: Drexel University, 2010.
105. Knirsch W, Kurtz C, Häffner N, Langer M, Kececioglu D. Normal values of the sagittal diameter of the lumbar spine (vertebral body and dural sac) in children measured by MRI. Pediatr Radiol. 2005; 35: 419–24. DOI: 10.1007/s00247-004-1382-6.

Литература

1. Degteva MO, Shagina NB, Vorobiova MI, Shishkina EA, Tolstykh EI, Akleyev AV. Contemporary Understanding of Radioactive Contamination of the Techa River in 1949–1956. Radiats Biol Radioecol. 2016; 56 (5): 523–34. PMID: 30703313.
2. Krestinina LY, Epifanova SB, Silkin SS, Mikryukova LD, Degteva MO, Shagina NB, Akleyev AV. Chronic low-dose exposure in the Techa River Cohort: risk of mortality from circulatory diseases. Radiat Environ Biophys. 2013; 52 (1): 47–57. DOI: 10.1007/s00411-012-0438-5.
3. Аклеев А. В. Хронический лучевой синдром у жителей прибрежных сел реки Теча. Челябинск: Книга, 2012; 464 с.
4. Preston DL, Sokolnikov ME, Krestinina LY, Stram DO. Estimates of radiation effects on cancer risks in the Mayak Worker, Techa River and Atomic Bomb Survivor Studies. Radiat Prot Dosimetry. 2017; 173 (1–3): 26–31. DOI: 10.1093/rpd/ncw316.
5. Degteva MO, Napier BA, Tolstykh EI, et al. Enhancements in the Techa River dosimetry system: TRDS-2016D Code for reconstruction of deterministic estimates of dose from environmental exposures. Health Phys. 2019; 117 (4): 378–87. DOI:10.1097/HP.0000000000001067.
6. Spiers FW, Beddoe AH, Whitwell JR. Mean skeletal dose factors for beta-particle emitters in human bone. Part I: volume-seeking radionuclides. The British journal of radiology. 1978; 51 (608): 622–7.
7. O'Reilly SE, DeWeese LS, Maynard MR, Rajon DA, Wayson MB, Marshall EL, et al. An 13 image-based skeletal dosimetry model for the ICRP reference adult female-internal electron 14 sources. Phys Med Biol. 2016; 61 (24): 8794–824.
8. Xu XG, Chao TC, Bozkurt A. VIP-Man: an image-based whole-body adult male model constructed from color photographs of the Visible Human Project for multi-particle Monte Carlo calculations. Health Phys. 2000; 78 (5): 476–86. DOI: 10.1097/00004032-200005000-00003. PMID: 10772019.
9. Shah AP, Bolch WE, Rajon DA, Patton PW, Jokisch DW. A paired-image radiation transport model for skeletal dosimetry. J Nucl Med. 2005; 46 (2): 344–53. PMID: 15695796.
10. Pafundi D. Image-based skeletal tissues and electron dosimetry models for the ICRP reference pediatric age series [dissertation]. Gainesville: University of Florida, 2009.
11. Hough M, Johnson P, Rajon D, Jokisch D, Lee C, Bolch W. An image-based skeletal dosimetry model for the ICRP reference adult male–internal electron sources. Phys Med Biol. 2011; 56 (8): 2309–46. DOI: 10.1088/0031-9155/56/8/001.
12. Bolch WE, Eckerman K, Endo A, et al. ICRP Publication 143: Paediatric Reference Computational Phantoms. Ann ICRP. 2020; 49 (1): 5–297. DOI: 10.1177/0146645320915031.
13. Degteva MO, Tolstykh EI, Shishkina EA, Sharagin PA, Zalyapin VI, Volchkova AY, et al. Stochastic parametric skeletal dosimetry model for humans: General approach and application to active marrow exposure from bone-seeking beta-particle emitters. PLoS ONE. 2021; 16 (10): e0257605. DOI: 10.1371/journal.pone.0257605.
14. Дёгтева М. О., Шишкина Е. А., Толстых Е. И., Заляпин В. И., Шарагин П. А., Смит М. А. и др. Методологический подход к разработке дозиметрических моделей скелета человека для бета-излучающих радионуклидов. Радиационная гигиена. 2019; 12 (2): 66–75. DOI: 10.21514/1998-426X-2019-12-2-66-75.
15. Volchkova AYu, Sharagin PA, Shishkina EA. Internal bone marrow dosimetry: the effect of the exposure due to 90Sr incorporated in the adjacent bone segments. Bulletin of the South Ural State

University. Ser. Mathematical Modelling, Programming & Computer Software. 2022; 15 (4): 44–58. DOI: 10.14529/mmp220404.
16. Шишкина Е. А., Шарагин П. А., Волчкова А. Ю. Аналитическое описание дозообразования в костном мозге от 90Sr, инкорпорированного в кальцифицированных тканях. Вопросы радиационной безопасности. 2021; 3: 72–82.
17. Силкин С. С., Крестинина Л. Ю., Старцев Н. В, Аклеев А. В. Уральская когорта аварийно-облученного населения. Медицина экстремальных ситуаций. 2019; 21 (3): 393–402.
18. Шарагин П. А., Шишкина Е. А., Толстых Е. И. Вычислительный фантом для дозиметрии красного костного мозга новорожденного ребенка от инкорпорированных бета-излучателей. Медицина экстремальных ситуаций. 2022; 4: 74–82. DOI: 10.47183/mes.2022.045.
19. Шарагин П. А., Шишкина Е. А., Толстых Е. И. Вычислительный фантом для дозиметрии красного костного мозга годовалого ребенка от инкорпорированных бета-излучателей. Медицина экстремальных ситуаций. 2023; 3: 44–55. DOI: 10.47183/mes.2023.030.
20. Cristy M. Active bone marrow distribution as a function of age in humans. Phys Med Biol. 1981; 26 (3): 389–400.
21. Sharagin PA, Shishkina EA, Tolstykh EI, Volchkova AYu, Smith MA, Degteva MO. Segmentation of hematopoietic sites of human skeleton for calculations of dose to active marrow exposed to bone-seeking radionuclides. RAD Conference Proceedings. 2018; 3: 154–8. DOI:10.21175/RadProc.2018.33.
22. Valentin J. Basic anatomical and physiological data for use in radiological protection: reference values. Annals of the ICRP. Annals of the ICRP. 2002; 32 (3–4): 1–277.
23. Woodard HQ and White DR. The composition of body tissues. Br. J. Ru&ol. 1986; 59: 1209–18.
24. Шарагин П. А., Толстых Е. И., Шишкина Е. А., Дегтева М. О. Дозиметрическое моделирование кости для остеотропных бета-излучающих радионуклидов: размерные параметры и сегментация. В сборнике: Материалы международной научной конференции «Современные проблемы радиобиологии»; 23–24 сентября 2021 г., Гомель, Беларусь. Современные проблемы радиобиологии – 2021. 2021; 200–4.
25. Толстых Е. И., Шарагин П. А., Шишкина Е. А., Дегтева М. О. Формирование доз облучения красного костного мозга человека от ^{89,90}Sr, оценка параметров трабекулярной кости для дозиметрического моделирования. В сборнике: Материалы международной научной конференции «Современные проблемы радиобиологии»; 23–24 сентября 2021 г., Гомель, Беларусь. Современные проблемы радиобиологии — 2021. 2021; 176–9.
26. Толстых Е. И., Шарагин П. А., Шишкина Е. А., Волчкова А. Ю. Дегтева М. О. Анатомо-морфологический базис для дозиметрического моделирования трабекулярной кости человека с использованием стохастического параметрического подхода. Клинический вестник ГНЦ ФМБЦ имени А. И. Бурназяна. 2022; 3: 25–40.
27. Shishkina EA, Timofeev YS, Volchkova AY, Sharagin PA, Zalyapin VI, Degteva MO, et al. Trabecula: a random generator of computational phantoms for bone marrow dosimetry. Health Phys. 2020; 118 (1): 53–9. DOI: 10.1097/HP.0000000000001127.
28. Zalyapin VI, Timofeev YuS, Shishkina EA. A parametric stochastic model of bone geometry. Bulletin of Southern Urals State University, Issue «Mathematical Modelling. Programming & Computer Software» (SUSU MMCS). 2018; 11 (2): 44–57. DOI: 10.14529/mmp180204.
29. Robinson RA. Chemical analysis and electron microscopy of bone. In: Rodahl K, Nicholson JT, Brown EM, editors. Bone as a tissue. New York: McGraw-Hill, 1960; p. 186–250.
30. Vogler JB 3rd, Murphy WA. Bone marrow imaging. Radiology. 1988; 168 (3): 679–93.
31. Vande Berg BC, Malghem J, Lecouvet FE, Maldague B. Magnetic resonance imaging of the normal bone marrow. Skeletal Radiology. 1998; 27: 471–83.
32. Vande Berg BC, Malghem J, Lecouvet FE, Maldague B. Magnetic resonance imaging of normal bone marrow. Eur Radiol. 1998; 8 (8): 1327–34.
33. Taccone A, Oddone M, Dell'Acqua AD, Occhi M, Ciccone MA. MRI «road-map» of normal age-related bone marrow. II. Thorax, pelvis and extremities. Pediatr Radiol. 1995; 25 (8): 596–606. PubMed PMID: 8570312.
34. Taccone A, Oddone M, Occhi M, Dell'Acqua AD, Ciccone MA. MRI «road-map» of normal age-related bone marrow. I. Cranial bone and spine. Pediatr Radiol. 1995; 25 (8): 588–95. PubMed PMID: 8570311.
35. Milovanovic P, Djonic D, Hahn M, Amling M, Busse B, Djuric M. Region-dependent patterns of trabecular bone growth in the human proximal femur: A study of 3D bone microarchitecture from early postnatal to late childhood period. Am J Phys Anthropol. 2017; 164 (2): 281–91. DOI: 10.1002/ajpa.23268.
36. Ryan TM, Krovitz GE. Trabecular bone ontogeny in the human proximal femur. J Hum Evol. 2006; 51 (6): 591–602.
37. Cunningham C, Scheuer L, Black S. Developmental Juvenile Osteology. 2rd ed. Elsevier Academic Press, 2016; p. 630.
38. Ryan TM, Raichlen DA, Gosman JH. Structural and mechanical changes in trabecular bone during early development in the human femur and humerus. Chapter 12. In: Percival CJ, Richtsmeier JT, editors. Building Bones: Bone Formation and Development in Anthropology. Cambridge University Press, 2017; p. 281–302.
39. Glorieux FH, Travers R, Taylor A, Bowen JR, Rauch F, Norman M, et al. Normative data for iliac bone histomorphometry in growing children. Bone. 2000; 26 (2): 103–9.
40. Volpato V. Bone endostructure morphogenesis of the human ilium. C. R. Palevol 7. 2008; 463–71. DOI: 10.1016/j.crpv.2008.06.001.
41. Rodriguez-Florez N, Ibrahim A, Hutchinson JC, Borghi A, James G, Arthurs OJ, et al. Cranial bone structure in children with sagittal craniosynostosis: Relationship with surgical outcomes. J Plast Reconstr Aesthet Surg. 2017; 70 (11): 1589–97. DOI: 10.1016/j.bjps.2017.06.017.
42. Gao S, Ren L, Qui R, Wu Z, Li C, Li J. Electron absorbed fractions in an image-based microscopic skeletal dosimetry model of chinese adult male. Radiat Prot Dosimetry. 2017; 175 (4): 450–9.
43. Pafundi D. Image-based skeletal tissues and electron dosimetry models for the ICRP reference pediatric age series [dissertation]. Gainesville: University of Florida, 2009.
44. Milenković P. Age Estimation Based on Analyses of Sternal End of Clavicle and the First Costal Cartilage Doctoral Dissertation [dissertation]. Belgrade: University Of Belgrade School of Medicine, 2013.
45. Kirmani S, Christen D, van Lenthe GH, Fischer PR, Bouxsein ML, McCready LK, et al. Bone structure at the distal radius during adolescent growth. J Bone Miner Res. 2009; 24 (6): 1033–42. DOI: 10.1359/jbmr.081255.
46. Mitchell DM, Caksa S, Yuan A, Bouxsein ML, Misra M, Burnett-Bowie SM. Trabecular bone morphology correlates with skeletal maturity and body composition in healthy adolescent girls. J Clin Endocrinol Metab. 2018; 103 (1): 336–45. DOI: 10.1210/jc.2017-01785.
47. Li X, Williams P, Curry EJ, Choi D, Craig EV, Warren RF, et al. Trabecular bone microarchitecture and characteristics in different regions of the glenoid. Orthopedics. 2015; 38 (3): 163–8.
48. Knowles NK, G Langohr GD, Faieghi M, Nelson A, Ferreira LM. Development of a validated glenoid trabecular density-modulus relationship. J Mech Behav Biomed Mater. 2019; 90: 140–5. DOI: 10.1016/j.jmbbm.2018.10.013.
49. Jun BJ, Vasanji A, Ricchetti ET, Rodriguez E, Subhas N, Li ZM, Iannotti JP. Quantification of regional variations in glenoid trabecular bone architecture and mineralization using clinical computed tomography images. J Orthop Res. 2018; 36 (1): 85–96. DOI: 10.1002/jor.23620.
50. Frich LH, Odgaard A, Dalstra M. Glenoid bone architecture J Shoulder Elbow Surg. 1998; 7 (4): 356–61.
51. Kneissel M, Roschger P, Steiner W, et al. Cancellous bone structure in the growing and aging lumbar spine in a historic Nubian population. Calcif Tissue Int. 1997; 61 (2): 95–100. DOI: 10.1007/s002239900302.
52. Arbabi A. A quantitative analysis of the structure of human sternum. J Med Phys. 2009; 34 (2): 80–6.
53. Bartl R, Frisch B. Biopsy of bone in internal medicine — an atlas and sourcebook. Dordrecht: Kluwer Academic Publishers, 1993; p. 250.

54. Baur-Melnyk A. Magnetic Resonance Imaging of the Bone Marrow. Springer Science & Business Media, 2012; p. 371.
55. Florence JL. Linear and cortical bone dimensions as indicators of health status in subadults from the Milwaukee County Poor Farm Cemetery. M. A.: University of Colorado at Denver, 2007.
56. Maresh MM. Measurements from roentgenograms. In: McCammon RW, editor. Human Growth and Development. Springfield, IL: Charles C. Thomas, 1970; p. 157–200.
57. Singh SP, Malhotra P, Sidhu LS, Singh PP. Skeletal frame size of spitian children. Journal of Human Ecology. 2007; 21 (3): 227–30.
58. Zivicnjak M, Smolej Narancić N, Szirovicza L, Franke D, Hrenović J, Bisof V, et al. Gender-specific growth patterns of transversal body dimensions in Croatian children and youth (2 to 18 years of age). Coll Antropol. 2008; 32 (2): 419–31. PubMed PMID: 18756891.
59. Свадовский Б. С. Возрастная перестройка костной ткани. О росте и развитии диафизов плечевой и бедренной костей. М.: Изд-во акад. пед. наук РСФСР, 1961; 110 с.
60. Miles AEW. Growth Curves of Immature Bones from a Scottish Island Population of Sixteenth to mid-Nineteenth Century: Limb-bone Diaphyses and Some Bones of the Hand and Foot. International Journal of Osteoarcheology. 1994; 4: 121–36.
61. Dhavale N, Halcrow SE, Buckley HR, Tayles N, Domett KM, Gray AR. Linear and appositional growth in infants and children from the prehistoric settlement of Ban Non Wat, Northeast Thailand: Evaluating biological responses to agricultural intensification in Southeast Asia, Journal of Archaeological Science: Reports. 2017; 11: 435–46. ISSN 2352-409.
62. Djurić M, Milovanović P, Djonić D, Minić A, Hahn M. Morphological characteristics of the developing proximal femur: a biomechanical perspective. Srp Arh Celok Lek. 2012; 140 (11–12): 738–45. PubMed PMID: 23350248.
63. Gosman JH, Ketcham RA. Patterns in ontogeny of human trabecular bone from SunWatch Village in the Prehistoric Ohio Valley: general features of microarchitectural change. Am J Phys Anthropol. 2009; 138 (3): 318–32. DOI: 10.1002/ajpa.20931. PubMed PMID: 18785633.
64. Petit MA, McKay HA, MacKelvie KJ, Heinonen A, Khan KM, Beck TJ. A randomized school-based jumping intervention confers site and maturity-specific benefits on bone structural properties in girls: a hip structural analysis study. J Bone Miner Res. 2002; 17 (3): 363–72. PubMed PMID: 11874228.
65. Danforth ME, Wrobel GD, Armstrong CW, Swanson D. Juvenile age estimation using diaphyseal long bone lengths among ancient Maya populations. Latin American Antiquity. 2017; 20 (1): 3–13.
66. Byers S, Moore AJ, Byard RW, Fazzalari NL. Quantitative histomorphometric analysis of the human growth plate from birth to adolescence. Bone. 2000; 27 (4): 495–501.
67. Beresheim AC, Pfeiffer S, Grynpas M. Ontogenetic changes to bone microstructure in an archaeologically derived sample of human ribs. J Anat. 2019; DOI: 10.1111/joa.13116.
68. Pfeiffer S. Cortical Bone Histology in Juveniles. Available from: https://www.researchgate.net/publication/303179375_Cortical_bone_histology_in_Juveniles.
69. Hresko AM, Hinchcliff EM, Deckey DG, Hresko MT. Developmental sacral morphology: MR study from infancy to skeletal maturity. Eur Spine J. 2020; 29 (5): 1141–6. DOI: 10.1007/s00586-020-06350-6.
70. Кузнецов Л. Е. Переломы таза у детей (морфология, биомеханика, диагностика). М.: Фолиум, 1994; 192 с.
71. Mavrych V, Bolgova O, Ganguly P and Kashchenko S. Age-related changes of lumbar vertebral body morphometry. Austin J Anat. 2014; 1 (3): 7.
72. Садофьева В. И. Нормальная рентгеноанатомия костно-суставной системы детей. Ленинград: Медицина, 1990; 216 с.
73. Bernert Zs, Évinger S, Hajdu T. New data on the biological age estimation of children using bone measurements based on historical populations from the Carpathian Basin. Annales Historico-Naturales Musei Nationalis Hungarici. 2007; 99: 199–206.
74. White TD, Black MT, Folkens PA. Human osteology: 3rd ed. Academic Press, 2011; p. 688.
75. Gindhart PS. Growth standards for the tibia and radius in children aged one month through eighteen years. Am J Phys Anthrop. 1973; 39: 41–8.
76. Lopez-Costas O, Rissech C, Trancho G, Turbón D. Postnatal ontogenesis of the tibia. Implications for age and sex estimation. Forensic Sci Int. 2012; 214 (1–3): 207.e1–11. DOI: 10.1016/j.forsciint.2011.07.038. PubMed PMID: 21862250.
77. Suominen PK, Nurmi E, Lauerma K. Intraosseous access in neonates and infants: risk of severe complications — a case report. Acta Anaesthesiol Scand. 2015; 59 (10): 1389–93. DOI: 10.1111/aas.12602. PubMed PMID: 26300243.
78. Blake KAS. An investigation of sex determination from the subadult pelvis: A morphometric analysis [dissertation]. Pittsburgh: University of Pittsburgh, 2011.
79. Cunningham CA, Black SM. Iliac cortical thickness in the neonate — the gradient effect. J Anat. 2009a; 215 (3): 364–70. DOI: 10.1111/j.1469-7580.2009.01112.x.
80. Cunningham CA, Black SM. Anticipating bipedalism: trabecular organization in the newborn ilium. J Anat. 2009b; 214 (6): 817–29. DOI: 10.1111/j.1469-7580.2009.01073.x.
81. Rissech C, Garcıa M, Malgosa A. Sex and age diagnosis by ischium morphometric analysis. Forensic Science International. 2003; 135: 188–96.
82. Rissech C, Malgosa A. Pubis growth study: Applicability in sexual and age diagnostic. Forensic Science International. 2007; 173: 137–45.
83. Corron L, Marchal F, Condemi S, Chaumoître K, Adalian P. A New Approach of Juvenile Age Estimation using Measurements of the Ilium and Multivariate Adaptive Regression Splines (MARS) Models for Better Age Prediction. Forensic Sci. 2017; 62 (1): 18–29. DOI: 10.1111/1556-4029.13224.
84. Parfitt AM, Travers R, Rauch F, Glorieux FH. Structural and cellular changes during bone growth in healthy children. Bone. 2000; 27 (4): 487–94. PMID: 11033443.
85. Schnitzler CM, Mesquita JM, Pettifor JM. Cortical bone development in black and white South African children: iliac crest histomorphometry. Bone. 2009; 44 (4): 603–11. DOI: 10.1016/j.bone.2008.12.009.
86. De Boer HH, Van der Merwe AE, Soerdjbalie-Maikoe VV. Human cranial vault thickness in a contemporary sample of 1097 autopsy cases: relation to body weight, stature, age, sex and ancestry. Int J Legal Med. 2016; 130 (5): 1371–7. DOI: 10.1007/s00414-016-1324-5.
87. Margulies S, Coats B. Experimental injury biomechanics of the pediatric head and brain. Chapter 4. In: Crandall J, Myers B, Meaney D, et al, editors. Pediatric Injury Biomechanics. New York: Springer Science+Business Media, 2013; p. 157–190.
88. Li Z, Park BK, Liu W, Zhang J, Reed MP, Rupp JD, et al. A statistical skull geometry model for children 0–3 years old. PLoS One. 2015; 10 (5). DOI: 10.1371/journal.pone.0127322.
89. Bleuze MM, Wheeler SM, Williams LJ, Dupras TL. Growth of the pectoral girdle in a sample of juveniles from the kellis 2 cemetery, Dakhleh Oasis, Egypt. Am J Hum Biol. 2016; 28 (5): 636–45.
90. McGraw MA, Mehlman CT, Lindsell CJ, Kirby CL. Postnatal growth of the clavicle: birth to eighteen years of age. Journal of Pediatric Orthopedics. 2009; 29: 937.
91. Bernat A, Huysmans T, Van Glabbeek F, Sijbers J, Gielen J, Van Tongel A. The anatomy of the clavicle: a three-dimensional cadaveric study. Clin Anat. 2014; 27 (5): 712–23.
92. Corron L. Juvenile age estimation in physical anthropology: A critical review of existing methods and the application of two standardised methodological approaches. Biological anthropology [dissertation]. Marseille: Aix-Marseille Universite, 2016.
93. Vallois HV. L'omoplate humaine. Bulletin de la Sociétié d'Anthropolgie de Paris. 1946; 7: 16–99.
94. Saunders S, Hoppa R, Southern R. Diaphyseal growth in a nineteenth-century skeletal sample of subadults from St Thomas' Church, Belleville, Ontario. International Journal of Osteoarchaeology. 1993; 3: 265–81.
95. Badr El Dine F, Hassan H. Ontogenetic study of the scapula among some Egyptians: Forensic implications in age and sex estimation using Multidetector Computed Tomography. Egyptian Journal of Forensic Sciences. 2015; 6 (2): 56–77.
96. Rissech C, Black S. Scapular development from neonatal period to skeletal maturity. A preliminary study. Int J Osteoarchaeol.

2007; 17: 451–64.
97. Bayaroğulları H, Yengil E, Davran R, Ağlagül E, Karazincir S, Balcı A. Evaluation of the postnatal development of the sternum and sternal variations using multidetector CT. Diagn Interv Radiol. 2014; 20 (1): 82–9.
98. Riach IC. Ossification in the sternum as a means of assessing skeletal age. J Clin Pathol. 1967; 20 (4): 589–90.
99. Johnson KT, Al-Holou WN, Anderson RC, Wilson TJ, Karnati T, Ibrahim M, et al. Morphometric analysis of the developing pediatric cervical spine. J Neurosurg Pediatr. 2016; 18 (3): 377–89. DOI: 10.3171/2016.3. PEDS1612. PubMed PMID: 27231821.
100. Caldas Md P, Ambrosano GM, Haiter Neto F. New formula to objectively evaluate skeletal maturation using lateral cephalometric radiographs. Braz Oral Res. 2007; 21 (4): 330–5. PubMed PMID: 18060260.
101. Peters JR, Chandrasekaran C, Robinson LF, Servaes SE, Campbell RM Jr, Balasubramanian S. Age- and gender-related changes in pediatric thoracic vertebral morphology. Spine J. 2015; 15 (5): 1000–20. DOI: 10.1016/j.spinee.2015.01.016.
102. Peters JR, Servaes SE, Cahill PJ, Balasubramanian S. Morphology and growth of the pediatric lumbar vertebrae. Spine J. 2021; 21 (4): 682–97. DOI: 10.1016/j.spinee.2020.10.029.
103. Newman SL, Gowland RL. The use of non-adult vertebral dimensions as indicators of growth disruption and non-specific health stress in skeletal populations. American journal of physical anthropology. 2015; 158 (1): 155–64.
104. Comeau A. Age-related changes in geometric characteristics of the pediatric thoracic cage and comparison of thorax shape with a Pediatric CPR Manikin [dissertation]. Philadelphia: Drexel University, 2010.
105. Knirsch W, Kurtz C, Häffner N, Langer M, Kececioglu D. Normal values of the sagittal diameter of the lumbar spine (vertebral body and dural sac) in children measured by MRI. Pediatr Radiol. 2005; 35: 419–24. DOI: 10.1007/s00247-004-1382-6.